



Strain-Induced Isomerization in One-Dimensional Metal–Organic Chains

Mykola Telychko⁺, Jie Su⁺, Aurelio Gallardo⁺, Yanwei Gu, Jesús I. Mendieta-Moreno, Dongchen Qi, Anton Tadich, Shaotang Song, Pin Lyu, Zhizhan Qiu, Hanyan Fang, Ming Joo Koh, Jishan Wu,* Pavel Jelínek* und Jiong Lu*

Abstract: The ability to use mechanical strain to steer chemical reactions creates completely new opportunities for solution- and solid-phase synthesis of functional molecules and materials. However, this strategy is not readily applied in the bottom-up on-surface synthesis of well-defined nanostructures. We report an internal strain-induced skeletal rearrangement of one-dimensional (1D) metal–organic chains (MOCs) via a concurrent atom shift and bond cleavage on Cu(111) at room temperature. The process involves Cu-catalyzed debromination of organic monomers to generate 1,5-dimethylnaphthalene diradicals that coordinate to Cu adatoms, forming MOCs with both homochiral and heterochiral naphthalene backbone arrangements. Bond-resolved non-contact atomic force microscopy imaging combined with density functional theory calculations showed that the relief of substrate-induced internal strain drives the skeletal rearrangement of MOCs via 1,3-H shifts and shift of Cu adatoms that enable migration of the monomer backbone toward an energetically favorable registry with the Cu(111) substrate. Our findings on this strain-induced structural rearrangement in 1D systems will enrich the toolbox for on-surface synthesis of novel functional materials and quantum nanostructures.

Introduction

On-surface synthesis of functional nanomaterials has attracted tremendous research interest because of its great potential for creating atomically precise functional nano-

structures with tailored electronic and magnetic properties.^[1–6] A common on-surface synthetic strategy involves thermal- or phototriggered chemical transformation of rationally designed molecular precursors on an appropriately chosen substrate.^[7] The future development in this field will hinge on the exploration of conceptually new toolkits that will enable precise steering of surface reactions under mild conditions to fabricate novel nanostructures with multiple functionalities.

Mechanochemical syntheses driven by the application of an external force or strain have emerged as promising and straightforward alternatives to traditional synthetic methods for fabricating functional organic molecules and nanomaterials. In addition to enabling advantageous solvent-free synthesis, mechanochemistry offers a completely new and efficient method for obtaining valuable products with high yield and selectivity.^[8] It would therefore be desirable to use mechanochemistry in bottom-up on-surface synthesis. Unfortunately, this is not straightforward because conventional methods for applying mechanical force, such as ball milling and cavity grinding, cannot be directly used with reactants adsorbed on surfaces.

As an alternative to standard mechanochemical methods, internal strain in molecular systems induced by interactions with a substrate could be used to mimic external mechanical stimuli. Recent studies have shown that substrate-induced structural distortion of molecular systems can facilitate their intra- and intermolecular cyclodehydrogenation as well as

[*] Dr. M. Telychko,^[†] J. Su,^[†] Y. Gu, S. Song, P. Lyu, Z. Qiu, H. Fang, Prof. M. J. Koh, Prof. J. Wu, Prof. J. Lu
Department of Chemistry, National University of Singapore
3 Science Drive 3, Singapore 117543 (Singapore)
E-Mail: chmwuj@nus.edu.sg
chmluj@nus.edu.sg

Dr. M. Telychko,^[†] J. Su,^[†] Prof. J. Lu
Centre for Advanced 2D Materials (CA2DM)
National University of Singapore
6 Science Drive 2, Singapore 117546 (Singapore)

A. Gallardo^[†]
Faculty of Mathematics and Physics, Charles University
V Holešovičkách 2, 180 00 Prague (Czech Republic)

A. Gallardo,^[†] J. I. Mendieta-Moreno, P. Jelínek
Institute of Physics, The Czech Academy of Sciences
162 00 Prague (Czech Republic)
E-Mail: jelinekp@fzu.cz

A. Gallardo,^[†] P. Jelínek
Regional Centre of Advanced Technologies and Materials
Palacký University
78371 Olomouc (Czech Republic)

D. Qi
School of Chemistry, Physics and Mechanical Engineering
Queensland University of Technology
Brisbane, Queensland 4001 (Australia)

Dr. A. Tadich
Australian Synchrotron
800 Blackburn Road, Clayton, Victoria 3168 (Australia)

Z. Qiu
NUS Graduate School for Integrative Sciences and Engineering
National University of Singapore
28 Medical Drive, Singapore 117456 (Singapore)

[†] These authors contributed equally to this work.

Supporting information and the ORCID identification number(s) for the author(s) of this article can be found under:
 <https://doi.org/10.1002/anie.201909074>.

skeletal rearrangements.^[9,10] Treirer et al. showed that van der Waals interactions between a polyphenylene precursor and a Cu(111) substrate tend to increase intramolecular strain, facilitating intramolecular cyclodehydrogenation and nanographene formation at elevated temperatures.^[9] Furthermore, Shiotari et al. found that the adsorption of a non-planar polycyclic hydrocarbon on Cu(100) induces the accumulation of internal strain, and that the relief of this strain at elevated temperatures promotes diverse skeletal rearrangements.^[10] It has also been reported that the substrate-binding affinity of equivalent chemical groups in organic molecules varies depending on their local adsorption geometries, enabling site-selective bond functionalization.^[11]

It is thus well established that strain energy stored in molecular systems on metallic substrates can be exploited to drive their chemical conversion into desired products. However, this phenomenon has primarily been studied in the context of chemical transformations of individual molecules. The use of substrate-induced internal strain to promote on-surface synthesis of extended nanostructures has not yet been studied systematically.

Herein, we demonstrate that strain relief in an extended 1D metal–organic chain (MOC) can drive extensive skeletal transformations at room temperature. The 1,5-dibromo-2,6-dimethylnaphthalene (DBDMN) precursor used in this work undergoes debromination upon deposition on a Cu(111) surface at room temperature, followed by the coordination of the resulting radicals to Cu adatoms to form self-assembled MOCs (Figure 1 a). Submolecular resolution imaging of these MOCs before and after strain relaxation was achieved using qPlus-based non-contact atomic force microscopy (nc-AFM)

with a carbon monoxide (CO)-functionalized tip. This showed that the strain-induced skeletal rearrangement of the MOCs involves a concurrent shift of Cu adatoms and H atoms accompanied by the migration of the monomer backbone toward an energetically favorable registry with the Cu(111) substrate. Theoretical calculations revealed the optimal reaction pathways for this process and the importance of entropic effects in the strain-driven skeletal transformations of 1D MOCs.

Results and Discussion

The DBDMN monomer was chosen as a precursor for MOC formation by deposition on a Cu(111) substrate. The synthesis and characterization of the purified DBDMN monomer are presented in the Supporting Information. As shown schematically in Figure 1 a, DBDMN has a naphthalene backbone with methyl groups at the 2 and 6 positions, and bromine atoms at the 1 and 5 positions. Adsorption on the Cu(111) surface was expected to induce facile cleavage of the C–Br bonds, forming σ -radicals (C(Br) radicals) that could coordinate with Cu adatoms to form MOCs. To test this hypothesis, we performed scanning tunneling microscopy (STM) on a Cu(111) surface after the deposition of DBDMN monomers at room temperature; this revealed the formation of 1D chain-like structures on Cu(111) (Figure 1 b). These 1D chains were often decorated by round protrusions, presumably because of the presence of Br adatoms released upon debromination and in keeping with previous results.^[12] Photoelectron spectroscopy experiments showed that the debromination of the DBDMN monomers occurred at room temperature and was accompanied by Cu–C bond formation and the emergence of MOCs (Supporting Information, Note 1, Figure S2). Room-temperature cleavage of the C–Br bonds of DBDMN on Cu(111) thus leads to the formation of 1D MOCs. Close-up STM images of representative MOCs showed that they contain only junctions formed by the heterochiral or homochiral coordination of neighboring DBDMN monomers (Figures 2 d,h). Conversely, samples subjected to prolonged (ca. 12 h) room-temperature annealing under ultrahigh vacuum (UHV) conditions formed a new type of 1D chain with distinct dumbbell-shaped junctions (Figure 1 c). This suggests that the initially formed MOCs underwent structural rearrangement during annealing—presumably because of substrate-induced strain. Throughout the manuscript, we refer to the MOCs obtained before and after room-temperature annealing as the „strained“ and „relaxed“ MOC isomers, respectively.

Structural characterization of strained MOCs. We initially probed the structures of the strained MOCs using STM and nc-AFM with a qPlus sensor. The nc-AFM imaging strategy used in this work relies on the functionalization of the tip with a CO molecule and the operation of the microscope in constant height mode in the short-range Pauli repulsion regime.^[13] The strongest Pauli repulsion occurs over regions of high electron density (for example, chemical bonds), which allows organic and metal–organic nanostructures to be imaged with submolecular resolution.^[14–17] Figure 2 shows

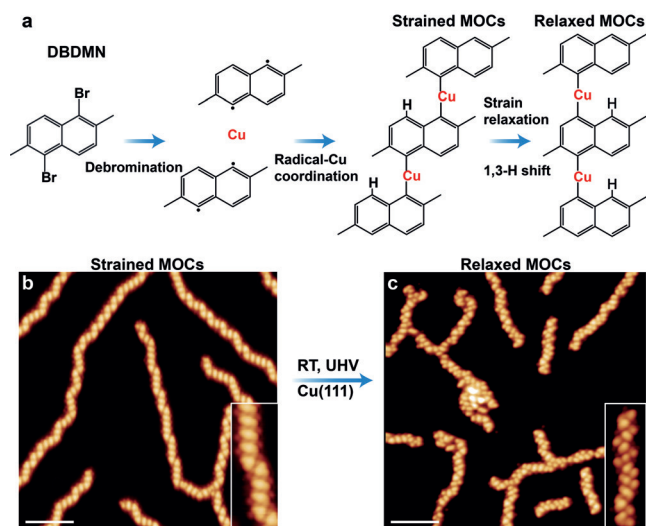


Figure 1. The skeletal rearrangement of MOCs on Cu(111). a) An illustration of the synthesis of MOCs and their structural relaxation on Cu(111). As-deposited DBDMN molecules undergo debromination and self-assemble into 1D MOCs. RT annealing leads to skeletal rearrangement of the MOC lattice. b,c) Large-scale STM topography images of 1D MOCs grown on Cu(111) before (b) and after (c) prolonged annealing under UHV at RT. The inset images show magnified views of representative strained and relaxed MOCs. Both images were acquired using tunneling parameters of 1 V, 1 nA; scale bars = 5 nm.

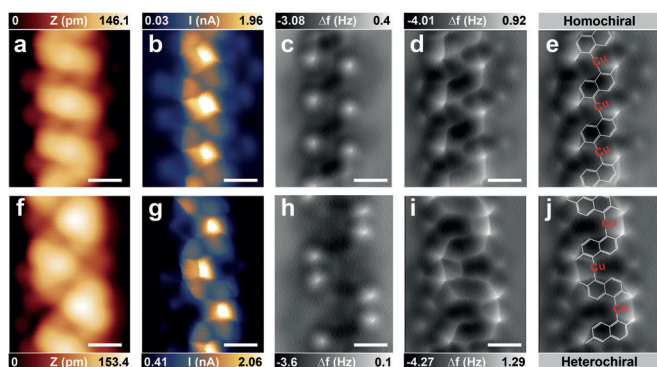


Figure 2. Structural characterization of strained MOCs. STM topography, constant height STM current, and nc-AFM images of a–e) homochiral and f–j) heterochiral MOC segments acquired using a CO tip. Tunneling parameters for STM topography images: 1 V, 1 nA. Constant height images were collected at tip-sample distances of +50 pm (d,i) and +100 pm (c,h) with respect to the set point of 50 mV, 1 nA; scale bars = 500 pm. Panel (e) and (j): the chemical structures of the MOCs superimposed over the nc-AFM images shown in (d) and (i).

STM topography, constant height current, and nc-AFM images of the strained homochiral (Figures 2a–e) and heterochiral (Figures 2f,j) MOC junctions. The bond-resolved nc-AFM images show a series of interconnected rectangular features with two bright apexes, which were assigned to the backbone of the individual DBDMN monomers and their methyl groups.

Nc-AFM images acquired with a larger tip-sample distance indicated that the methyl groups exhibited the strongest Pauli repulsion (Figures 2c,h). The faint lines linking adjacent molecules via the carbon atoms originally bound to Br (1 and 5) exhibit the highest STM contrast. Similar enhancements of STM contrast over coordinated adatoms have been reported for multiple metal–organic systems.^[18–20] These observations indicate that σ -radicals formed by cleaving the C–Br bonds in DBDMN coordinate to Cu adatoms, forming 1D MOCs. We also resolved the Cu(111) lattice around the MOCs, revealing the adsorption geometry of the Cu adatoms in the chains. The Cu adatoms predominantly occupy bridge sites along the high-symmetry [110] lattice direction (Supporting Information, Note 3, Figure S6).

We performed DFT calculations to better understand the structures of the strained MOCs. These calculations indicated that the DBDMN monomers lie approximately 2.25 Å above the Cu(111) surface. Moreover, each DBDMN monomer adopts a bent configuration such that its methyl groups are lifted above the naphthalene backbone (Figure 3e). To enable direct comparison between the DFT results and experimental data, we generated simulated nc-AFM images of the DFT-relaxed models using a modified probe–particle model developed by Hapala et al.^[21–23] The out-of-plane bending of the DBDMN monomer precludes direct visualization of the naphthalene rings' internal structure. Nevertheless, the calculated nc-AFM image (Figure 3d) exhibits all the characteristic features of our experimental images, including the bright features related to methyl groups. Additionally, the C–Cu–C coordination bonds are visible as distinct line features in the

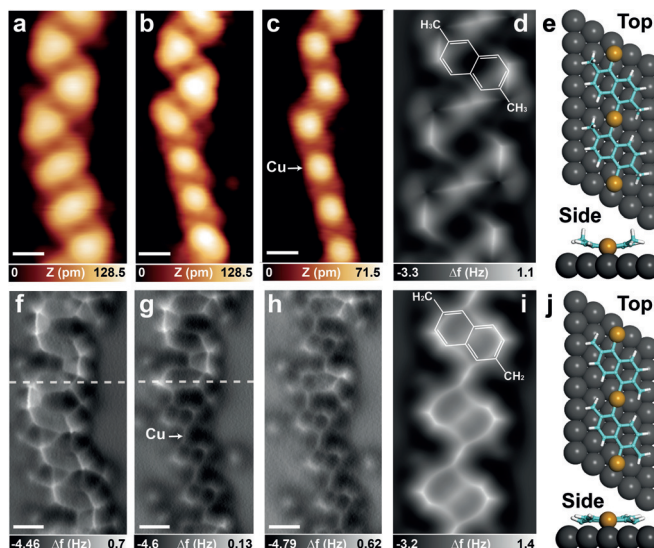


Figure 3. Tip-assisted dehydrogenation of methyl groups. STM topography and the corresponding constant height nc-AFM images of a,f) the strained MOC and the same MOC with b,g) partially and c,h) fully dehydrogenated methyl groups. d,i) Simulated nc-AFM images of a homochiral MOC with and without dehydrogenated methyl groups, respectively. e,j) DFT-optimized models showing the conformations of two adjacent DBDMN backbones before and after tip-assisted dehydrogenation of their methyl groups, respectively. STM topography images were acquired using tunneling parameters of 1 V, 1 nA. Constant height images were collected at tip-sample distances of +50 pm (f), +70 pm (g), and +50 pm (h) with respect to a setpoint of 20 mV, 1 nA.

simulated nc-AFM images, and in good agreement with the experimental data. All these observations support the proposed model of the strained MOCs. AFM images of heterochiral MOCs also exhibited sharp line features linking methyl groups of adjacent DBDMN molecules. These line features are not attributed to the presence of chemical bonds but to the close proximity of the $-\text{CH}_3$ groups, which create sharp ridges in the potential energy landscape that induce bending of the CO probe–particle.^[21]

Tip-induced dehydrogenation of methyl groups. Multiple STM imaging sessions involving scanning at a bias voltage (V_s) of $V_s \geq 1.6$ V induced irreversible structural changes in the MOCs. By acquiring a series of STM and nc-AFM images, we were able to capture the structural evolution of individual MOCs after stepwise scanning at $V_s = 2$ V (Figure 3). We first performed STM imaging of the lower part of a strained MOC at $V_s = 2$ V to trigger tip-induced structural change. We then switched to a constant height nc-AFM imaging to capture structural changes in the MOCs (Figures 3b,g).

The naphthalene rings of each DBDMN monomer become well resolved in the nc-AFM images of the partially dehydrogenated MOC (Figure 3g), and the line feature (indicated by a white arrow) associated with the C–Cu–C bond was more clearly visible than in the corresponding image of the parent strained MOC. Applying the same imaging protocol (scanning at $V_s = 2$ V) to the upper part of this MOC caused the STM and nc-AFM contrast to become uniform over the entire MOC backbone (Figures 3c,h). These

observations indicate that the methyl groups ($-\text{CH}_3$) of the DBDMN monomers underwent monodehydrogenation to produce $-\text{CH}_2$ radicals, leading to changes in both STM and nc-AFM contrast. We therefore performed DFT calculations for a new MOC structure in which the DBDMN monomers have monodehydrogenated methyl groups ($-\text{CH}_2$) and a planar molecular adsorption geometry (Figure 3j).

The experimental nc-AFM images of the dehydrogenated homochiral MOC are reproduced well by their simulated counterpart (Figure 3i). Interestingly, dehydrogenation has no appreciable effect on the spatial locations of intramolecular features and therefore clearly does not induce intermolecular rearrangements or affect the C–Cu–C bonding motif. Moreover, the dehydrogenation of $-\text{CH}_3$ groups enables direct visualization of the C–Cu–C bond, as evidenced by the sharp lines connecting the DBDMN backbone units. We could thus use this tip-controlled dehydrogenation technique to elucidate the mechanism of the isomeric transformation of the MOCs.

Structural characterization of relaxed MOCs. After prolonged room-temperature annealing under UHV conditions, the MOCs undergo a structural rearrangement and adopt a new relaxed isomeric form. To illustrate the structural rearrangements that occur during this process, we conducted STM and nc-AFM imaging of a partially relaxed MOC before (Figures 4a–c) and after (Figures 4d,e) dehydrogenation of methyl groups. The lower part of this MOC consists predominantly of strained homochiral junctions, while the upper part features a series of dumbbell-shaped junctions (indicated by white arrows in Figure 4a), presumably because of the presence of a distinct C–Cu–C coordination bonding motif. Bond-resolved nc-AFM images (Figure 4e) of the same dehydrogenated MOC show that each dumbbell-shaped junction consists of one Cu adatom coordinated to one C(Br) σ -radical site and one C(H) σ -radical site. Conversely, in the strained homochiral MOC junctions each Cu adatom is

coordinated to two C(Br) σ -radical sites. These different coordination motifs can be seen by examining representative homochiral MOC junctions in the strained (Figure 4f) and relaxed isomeric configurations (Figure 4g; for an image of a representative MOC with a higher degree of relaxation see the Supporting Information, Note 4).

Our bond-resolved nc-AFM images provided several deep insights into the structural transformation that relaxes the strained MOC upon room-temperature annealing. First, they showed that the relaxed MOC junctions could be derived from the strained homochiral or heterochiral MOCs by a shift of the Cu coordination center from C(Br) to an adjacent C(H) site together with the shift of a H atom from the C(H) to the formerly Cu-bound C(Br) site (Figure 1a). Second, the strained and relaxed MOCs exhibit different registries with respect to the Cu(111) lattice. The Cu adatoms in the strained MOC are aligned along the [110] direction whereas those in the relaxed MOCs align with a twist angle of about 20° relative to the strained MOC. The alignments of the two MOC types are indicated by the dashed white lines in Figure 4e. Third, the average separations between adjacent Cu coordination centers (that is, the Cu–Cu distances) were $7.6 \pm 0.093 \text{ \AA}$ and $6.91 \pm 0.085 \text{ \AA}$ for the strained and relaxed MOCs, respectively. The Cu adatoms tended to occupy the bridge sites of Cu(111). Therefore, the difference in the Cu–Cu distances observed for the two MOC types is tentatively attributed to the different interstitial separations of bridge sites along distinct lattice directions.

The substantial difference in the separation of nearest neighbor Cu atoms in the two MOC types indicates that the strain in the initial MOC may be the driving force of its isomeric transformation. To test this hypothesis, we used DFT to compute the total energies of the two MOC isomers with and without the Cu(111) substrate. The total energy difference between strained and relaxed freestanding MOC isomers is negligible (ca. 15 meV; Supporting Information, Note 6). Therefore, the energy gain as a consequence of electronic effects arising from the change in the binding configuration of the Cu adatoms and the naphthalene skeleton does not contribute significantly to the induction of isomerization. We also analyzed the Cu–Cu distances between nearest neighbor Cu adatoms in the optimized free-standing and surface-supported homochiral MOCs. This revealed that the Cu–Cu distance increases from 7.2 \AA in the freestanding strained isomer to 7.67 \AA in the surface-supported MOC. Conversely, the Cu–Cu distances in the freestanding and surface-supported relaxed MOC are 6.73 \AA and 6.99 \AA , respectively. Surface adsorption thus substantially increases the Cu–Cu distance in the strained MOC isomer (by 0.47 \AA), indicating that the strain energy is probably stored in the elongated C–Cu–C coordination bonds. The calculations also show that the total energy of the relaxed MOC isomer on Cu(111) is approximately 0.28 eV lower than that of its strained counterpart. The transformation into the relaxed MOC isomeric configuration

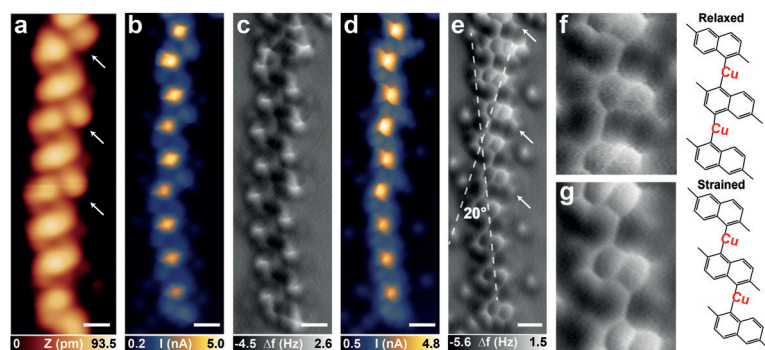


Figure 4. Probing strain-induced MOC relaxation. a) STM topography image of a partially relaxed MOC. b,c) Constant height STM current and nc-AFM images of the same MOC. d,e) Constant height STM current and nc-AFM images of the same MOC after methyl group dehydrogenation. f,g) Magnified view of the relaxed and strained homochiral MOC segments with the corresponding atomic models. The dashed white lines in image (e) indicate the differing registration of the relaxed and strained MOC segments with respect to the Cu(111) substrate. The STM topography image (a) was recorded using tunneling parameters of 1 V, 1 nA. Constant height images were collected at tip-sample distances of +100 pm (b,d) and +50 pm (c,e) with respect to a setpoint of 50 mV, 1 nA.

is thus favored because it minimizes the system's total energy.

Isomerization pathway. We explored multiple pathways for the isomerization process (Supporting Information, Note 6, Figure S11). A process involving a 1,3-H atom shift with a concomitant reorganization of the coordinate bonding from C(Br)–Cu–C(Br) to C(Br)–Cu–C(H) was found to be the most feasible of the considered possibilities. To obtain deeper insights into the reaction mechanism, we performed quantum mechanics/molecular mechanics (QM/MM) molecular dynamics (MD) simulations^[24] to determine the free energy profile of reaction steps that might contribute to these skeletal rearrangements (Figure 5). These calculations also provided insight into the effect of temperature on the transformation mechanism, which was important (Supporting Information, Note 5). To identify the most feasible pathway, we considered various reaction coordinates for the first step of the process (for other possible pathways see the Supporting Information, Figure S11). Because the calculations were computationally expensive, only homochiral MOC junctions were considered. Figure 5 shows the reaction pathway for the isomeric relaxation of MOCs with the lowest activation energy according to our simulations. This pathway involves a two-step process with two activation barriers (Figure 5g). The first step is a rapid 1,3-H shift described by the $\delta H = h_3 - h_1$ reaction coordinate (Figure 5f). The shift presumably proceeds by translocation of the H atom on C3 onto the Cu adatom followed by addition across the C1–Cu bond via the transient structure depicted in Figure 5b; this process has a computed activation barrier of 1.18 eV. It may seem difficult to overcome such a barrier at 300 K. However, the reaction

rate Γ is given by the expression $\Gamma = \nu e^{-\Delta F/kT}$, where ΔF is the free energy barrier, T is the temperature, k is Boltzmann's constant, and ν is the effective frequency associated with the vibrations in the direction of the reaction path.^[25] In our case, the catalytic effect of the mechanical strain enhances these vibrational modes and thus increases the transition rate, facilitating the reaction. The subsequent rearomatization of the naphthalene backbone is accompanied by weakening of the C1–Cu bond and the formation of a new C3–Cu bond (Figure 5c). The energy of the resulting system is 0.5 eV higher than that of the initial state. Notably, the 1,3-H migration and formation of the C3–Cu bond are facilitated by thermal fluctuations in the vertical position of the Cu adatom (see the red curve in Figure 5h), which reduces the free energy barrier. During this step, the Cu adatom also migrates to an adjacent bridge site on the Cu(111) surface (Figures 5c,d). The isomerization is completed by the dissociation of the bond between the Cu adatom and the C1 atom (Supporting Information, Figure S9). Using this bond distance as a reaction coordinate, $\Delta(\text{Cu}-\text{C})$, we traced the system's transformation to its final state (Figure 5e) and showed that it involves overcoming an activation barrier of 0.78 eV (Figure 5d). The dissociation of this bond allows the system to reach the relaxed configuration by releasing the stress of the intermediate structure. Importantly, our calculations also reveal a vertical movement of approximately 0.4 Å of the whole naphthalene unit as a consequence of the activation of out-of-plane molecular vibration modes at elevated temperatures. The temperature-induced vertical movement facilitates the reaction greatly by lowering the activation barrier. This clearly illustrates the importance of performing free energy calculations at elevated temperatures when seeking to correctly describe on-surface reaction mechanisms and the associated entropic effects.

C–Cu–C bond cleavage and C–H bond activation on catalytically active substrates typically require thermal treatment at over 400 K.^[26–29] They are often followed by direct C–C coupling, leading to the formation of graphene-like nanostructures.^[5,6] However, unlike the 2D MOC networks reported previously, the 1D strained MOCs studied here undergo C–Cu–C bond cleavage at room temperature as part of a complex reaction driven by the relief of substrate-induced strain.

Conclusion

In summary, we have demonstrated a strain-induced structural rearrangement of 1D MOCs on a Cu(111) surface at room temperature. Our results show that strain relief drives the skeletal rearrangement of MOCs, which involves concurrent rearrangements of Cu adatoms and H atoms together with the migration of monomers toward an energetically favorable registry on the Cu(111) substrate. This process is facilitated at elevated

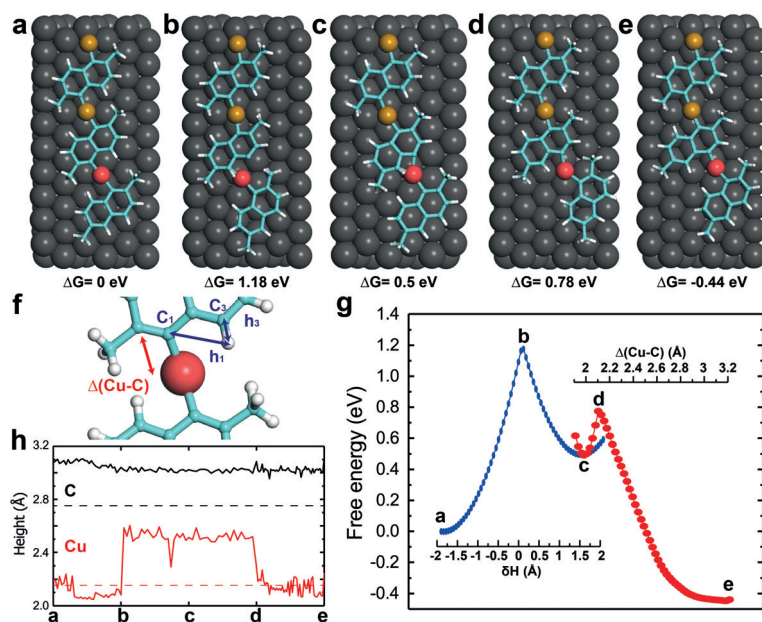


Figure 5. Free energy calculation for the proposed reaction pathways. a–e) Top view of the structures at different stages of the reaction. f) A depiction of important distances and the atoms participating in the reaction. h) Height of the Cu adatom (red) and average heights of the C atoms (black) during the reaction at 300 K; the heights of the corresponding atoms in the relaxed structure at 0 K are shown by the dashed lines. g) Free energy profile of the two-step reaction. The first part goes through the reaction coordinate $\delta H = h_3 - h_1$ and the second part through $\Delta(\text{Cu}-\text{C})$.

temperatures by the vertical displacement of the MOC's organic backbone because of the activation of the out-of-plane vibrational modes. Theoretical calculations showed that the optimal reaction pathway is highly sensitive to entropic effects, illustrating the importance of performing free energy calculations at elevated temperatures when studying on-surface reaction mechanisms. These results may support the development of new strategies for fabricating functional materials and quantum nanostructures to be used in both fundamental research and new technologies.

Experimental Section

STM/nc-AFM measurements were performed on a commercial Omicron machine using a qPlus sensor with a resonant frequency of 28.2 kHz, quality factor of $Q = 10\,500$ and oscillation amplitude of 100 pm, operated in frequency-modulation mode.^[30] DFT calculations were performed using the FHI-AIMS code.^[31] All geometric optimizations were performed at the GGA-PBE^[32] level, using light wave functions and the Tkatchenko–Scheffler^[33] treatment of van der Waals interactions. We also used a QM/MM method, Fireball/Amber,^[24] that combines classical force field techniques as implemented in Amber^[34] with local orbital DFT calculations performed with Fireball.^[35] The MM computations were performed using the interface force-field^[36] and the DFT calculations used the BLYP exchange-correlation functional^[37,38] with D3 corrections^[39] and norm-conserving pseudopotentials together with a basis set of optimized numerical atomic-like orbitals.^[40] The free energy profile was generated using the WHAM method.^[41] Extended experimental and computational details are presented in the Supporting Information.

Acknowledgements

J.L. acknowledges the support from MOE Tier 2 grants (R-143-000-A06-112, R-143-000-682-112, and R-143-000-A75-114). P.J. acknowledges support from Praemium Academic of the Czech Academy of Sciences, the Ministry of Education of the Czech Republic Grant LM2015087 and GACR project No. 18–09914S. J.W. acknowledges financial support from the MOE Tier 3 program (MOE2014-T3-1–004). D.Q. acknowledges the support of the Australian Research Council (Grant No. FT160100207). Part of this research was undertaken on the Soft X-ray spectroscopy beamline at the Australian Synchrotron, part of ANSTO.

Conflict of interest

The authors declare no conflict of interest.

Stichwörter: Debromierung · Isomerisierung · Metall-organische Strukturen · Rasterkraftmikroskopie · Rastertunnelmikroskopie

Zitierweise: *Angew. Chem. Int. Ed.* **2019**, *58*, 18591–18597
Angew. Chem. **2019**, *131*, 18764–18770

- [1] C. Janiak, J. K. Vieth, *New J. Chem.* **2010**, *34*, 2366.
- [2] S. Stepanow, N. Lin, J. V. Barth, *J. Phys. Condens. Matter* **2008**, *20*, 184002.
- [3] M. Di Giovannantonio, M. El Garah, J. Lipton-Duffin, V. Meunier, L. Cardenas, Y. Fagot Revurat, A. Cossaro, A. Verdini, D. F. Perepichka, F. Rosei, G. Contini, *ACS Nano* **2013**, *7*, 8190.
- [4] L. Grill, M. Dyer, L. Lafferentz, M. Persson, M. V. Peters, S. Hecht, *Nat. Nanotechnol.* **2007**, *2*, 687.
- [5] J. Cai, P. Ruffieux, R. Jaafar, M. Bieri, T. Braun, S. Blankenburg, M. Muoth, A. P. Seitsonen, M. Saleh, X. Feng, K. Müllen, R. Fasel, *Nature* **2010**, *466*, 470.
- [6] L. Talirz, P. Ruffieux, R. Fasel, *Adv. Mater.* **2016**, *28*, 6222.
- [7] S. Clair, D. G. de Oteyza, *Chem. Rev.* **2019**, *119*, 4717.
- [8] J. L. Howard, Q. Cao, D. L. Browne, *Chem. Sci.* **2018**, *9*, 3080.
- [9] M. Treier, C. A. Pignedoli, T. Laino, R. Rieger, K. Müllen, D. Passerone, R. Fasel, *Nat. Chem.* **2011**, *3*, 61.
- [10] A. Shiotari, T. Nakae, K. Iwata, S. Mori, T. Okujima, H. Uno, H. Sakaguchi, Y. Sugimoto, *Nat. Commun.* **2017**, *8*, 16089.
- [11] Q. Zhong, D. Ebeling, J. Tschakert, Y. Gao, D. Bao, S. Du, C. Li, L. Chi, A. Schirmeisen, *Nat. Commun.* **2018**, *9*, 3277.
- [12] J. Liu, B. Xia, H. Xu, N. Lin, *J. Phys. Chem. C* **2018**, *122*, 13001.
- [13] L. Gross, F. Mohn, N. Moll, P. Liljeroth, G. Meyer, *Science* **2009**, *325*, 1110.
- [14] D. G. de Oteyza, P. Gorman, Y.-C. Chen, S. Wickenburg, A. Riss, D. J. Mowbray, G. Etkin, Z. Pedramrazi, H.-Z. Tsai, A. Rubio, M. F. Crommie, F. R. Fischer, *Science* **2013**, *340*, 1434.
- [15] S. Kawai, A. Sadeghi, T. Okamoto, C. Mitsui, R. Pawlak, T. Meier, J. Takeya, S. Goedecker, E. Meyer, *Small* **2016**, *12*, 5303.
- [16] N. Kocić, X. Liu, S. Chen, S. Decurtins, O. Krejčí, P. Jelínek, J. Repp, S.-X. Liu, *J. Am. Chem. Soc.* **2016**, *138*, 5585.
- [17] F. Queck, O. Krejčí, P. Scheuerer, F. Bolland, M. Otyepka, P. Jelínek, J. Repp, *J. Am. Chem. Soc.* **2018**, *140*, 12884.
- [18] W. Wang, X. Shi, S. Wang, M. A. Van Hove, N. Lin, *J. Am. Chem. Soc.* **2011**, *133*, 13264.
- [19] Q. Sun, L. Cai, S. Wang, R. Widmer, H. Ju, J. Zhu, L. Li, Y. He, P. Ruffieux, R. Fasel, W. Xu, *J. Am. Chem. Soc.* **2016**, *138*, 1106.
- [20] J. Liu, Q. Chen, K. Cai, J. Li, Y. Li, X. Yang, Y. Zhang, Y. Wang, H. Tang, D. Zhao, K. Wu, *Nat. Commun.* **2019**, *10*, 2545.
- [21] P. Hapala, G. Kichin, C. Wagner, F. S. Tautz, R. Temirov, P. Jelínek, *Phys. Rev. B* **2014**, *90*, 085421.
- [22] P. Hapala, M. Švec, O. Stetsovych, N. J. van der Heijden, M. Ondráček, J. van der Lit, P. Mutombo, I. Swart, P. Jelínek, *Nat. Commun.* **2016**, *7*, 11560.
- [23] O. Krejčí, P. Hapala, M. Ondráček, P. Jelínek, *Phys. Rev. B* **2017**, *95*, 045407.
- [24] J. I. Mendieta-Moreno, R. C. Walker, J. P. Lewis, P. Gómez-Puertas, J. Mendieta, J. Ortega, *J. Chem. Theory Comput.* **2014**, *10*, 2185.
- [25] G. H. Vineyard, *J. Phys. Chem. Solids* **1957**, *3*, 121.
- [26] Q. Li, B. Yang, J. Björk, Q. Zhong, H. Ju, J. Zhang, N. Cao, Z. Shi, H. Zhang, D. Ebeling, A. Schirmeisen, J. Zhu, L. Chi, *J. Am. Chem. Soc.* **2018**, *140*, 6076.
- [27] L. Ferrighi, I. Piš, T. H. Nguyen, M. Cattelan, S. Nappini, A. Basagni, M. Parravicini, A. Papagni, F. Sedona, E. Magnano, F. Bondino, C. Di Valentin, S. Agnoli, *Chem. Eur. J.* **2015**, *21*, 5826.
- [28] Q. Fan, S. Werner, J. Tschakert, D. Ebeling, A. Schirmeisen, G. Hilt, W. Hieringer, J. M. Gottfried, *J. Am. Chem. Soc.* **2018**, *140*, 7526.
- [29] M. Fritton, K. Otte, J. Björk, P. K. Biswas, W. M. Heckl, M. Schmittel, M. Lackinger, *Chem. Commun.* **2018**, *54*, 9745.
- [30] F. J. Giessibl, *Appl. Phys. Lett.* **1998**, *73*, 3956.
- [31] V. Blum, R. Gehrke, F. Hanke, P. Havu, V. Havu, X. Ren, K. Reuter, M. Scheffler, *Comput. Phys. Commun.* **2009**, *180*, 2175.
- [32] J. P. Perdew, K. Burke, M. Ernzerhof, *Phys. Rev. Lett.* **1996**, *77*, 3865.
- [33] A. Tkatchenko, M. Scheffler, *Phys. Rev. Lett.* **2009**, *102*, 073005.

- [34] D. A. Case, I. Y. Ben-Shalom, S. R. Brozell, D. S. Cerutti, T. E. Cheatham III, V. W. D. Cruzeiro, T. A. Darden, R. E. Duke, D. Ghoreishi, M. K. Gilson, et al., *AMBER 2018*, University of California, San Francisco 2018.
- [35] J. P. Lewis, P. Jelínek, J. Ortega, A. A. Demkov, D. G. Trabada, B. Haycock, H. Wang, G. Adams, J. K. Tomfohr, E. Abad, H. Wang, D. A. Drabold, *Phys. Status Solidi B* **2011**, *248*, 1989.
- [36] H. Heinz, T. J. Lin, R. Kishore Mishra, F. S. Emami, *Langmuir* **2013**, *29*, 1754.
- [37] A. D. Becke, *Phys. Rev. A* **1988**, *38*, 3098.
- [38] C. Lee, W. Yang, R. G. Parr, *Phys. Rev. B* **1988**, *37*, 785.
- [39] S. Grimme, S. Ehrlich, L. Goerigk, *J. Comput. Chem.* **2011**, *32*, 1456.
- [40] M. Basanta, Y. Dappe, P. Jelínek, J. Ortega, *Comput. Mater. Sci.* **2007**, *39*, 759.
- [41] S. Kumar, J. M. Rosenberg, D. Bouzida, R. H. Swendsen, P. A. Kollman, *J. Comput. Chem.* **1992**, *13*, 1011.

Manuskript erhalten: 20. Juli 2019

Veränderte Fassung erhalten: 21. September 2019

Akzeptierte Fassung online: 13. Oktober 2019

Endgültige Fassung online: 4. November 2019